Supporting Information (SI) for:

Advantageous Crystalline-Amorphous Phase Boundary for Enhanced Electrochemical Water Oxidation

HyukSu Han,†[a] Heechae Choi,†[b] Sungwook Mhin,†[c] Yu-Rim Hong,[d] Kang Min Kim,[d] Jiseok Kwon,[e] Ghulam Ali,[f,g] Kyung Yoon Chung,[g] Minyoung Je,[b] Ha Nee Umh,[h] Dong-Ha Lim,[h] Kenneth Davey,[h] Shi-Zhang Qiao,*[h] Ungyu Paik,*[e] Taeseup Song*[e]

[a]*Department of Materials Science and Engineering, Hongik University, Sejong-ro 2639, Sejong, Republic of Korea*

[b]*Institute of Inorganic Chemistry, University of Cologne, Greinstr. 6, 50939, Cologne, Germany*

[c]*Korea Institute of Industrial Technology, Gaetbeol-ro 156, Yeonsu-gu, Incheon 21999, Republic of Korea*

[d]*Korea Institute of Industrial Technology, 137-41 Gwahakdanji-ro, Gangneung-si, Gangwon-do 25440, Republic of Korea*

[e]*Department of Energy Engineering, Hanyang University, Seoul 04763, Republic of Korea*

[f]*Department of Physics, University of the Punjab, Lahore, 54590, Pakistan.*

[g]*Center for Energy Storage Research, Korea Institute of Science and Technology, Hwarang-ro 14-gil 5, Seongbuk-gu, Seoul 02792, Republic of Korea*

[h] *Korea Institute of Industrial Technology (KITECH), 42-7 Baegyang-daero 804beon-gil, Sasang-gu, Busan, 46938, Republic of Korea*

[i]*School of Chemical Engineering, The University of Adelaide, Adelaide, SA 5005, Australia*

† These authors contributed equally to this work.

Emails: S.Z. Qiao (s.qiao@adelaide.edu.au); U. Paik (upaik@hanyang.ac.kr); T. Song

(tssong@hanyang.ac.kr)

EXPERIMENTAL SECTION

***Catalyst Preparation (Co_2B and F-Co_2B)*:** All chemicals were purchased from Sigma-Aldrich and used without further purification. To prepare Co_2B powder, a solution of cobalt chloride ($CoCl_2 \cdot 6H_2O$, 20 mL, concentration 0.5 M) in a round-bottomed flask was flushed with argon for de-aeration and maintained at 0˚C in an ice-bath. A 1.0 M sodium borohydride ($NaBH_4$) in 0.1 M sodium hydroxide (NaOH) was prepared separately and added drop-wise using a syringe to the $CoCl_2$ solution. A dark precipitate was instantaneously formed that was collected by filtration. The collected precipitate was washed with distilled (DI) water and ethanol several times and stored in vacuum-oven for 24 h. The dried-powder was subjected to pyrolysis at 600 ˚C under argon for 2 h. For F-Co_2B, appropriate amounts of ammonium fluoride (NH_4F) were mixed with $CoCl_2$ solution, and preparation was identical with that for Co_2B.

***Catalyst Characterizations*:** Field-emission **s**canning electron microscopy (FE-SEM; model S4800; Hitachi) was used to study the surface morphologies of the samples. Transmission electron microscopy (TEM; Talos F200X; Thermo Fisher Scientific) equipped with an energy dispersive X-ray (EDX) was used to acquire TEM, and elemental mapping, images. Structural characterization was determined by X-ray diffraction (XRD; D/MAX-2500/PC; Rigaku) patterns using a diffractometer with Cu-Kα radiation ($\lambda = 0.15418$ nm) at 40 kV and 100 mA. The surface electronic states and composition of the samples, were analyzed by X-ray photoelectron spectroscopy (XPS; VG ESCALAB 200i; Thermo Fisher Scientific). XPS survey and high-resolution scans were conducted with pass energies of, respectively, 100 and 20 eV.

***Electrochemical Measurements*:** The electrochemical performance of the catalysts was evaluated in 1.0 M KOH using a three-electrode electrochemical cell with a rotating disk electrode (RDE) which was controlled by an electrochemistry workstation (Autolab PGSTAT; Metrohm). Titration vessel (height: 80 mm, outer diameter: 78 m, volume: 90 ml) made by clear glass was used as a testing cell. The distance between working and reference electrodes was about 1 cm. In a typical preparation of the working electrode, a powder of 4 mg was dispersed in a Nafion® solution (30 μL, 5 wt.%) of water (1 mL) and ethanol (volume ratio 3:1). A homogeneous ink formed after 20 min ultrasonication. A 5 μL of the catalyst ink was drop-cast onto the surface of a glassy-carbon (GC) RDE electrode which had a diameter of 3 mm to yield a catalyst loading of 0.285 mg cm^{-2}. The working electrode was air-dried for 24 h under ambient conditions. The electrolyte was purged with O_2 before measurements. During measurement the RDE electrode was rotated at 2,000 rpm to remove any bubbles. Hg/HgO and graphite rod were used, respectively, as the reference electrode and counter electrode. Prior to electrochemical measurement the working electrode was subjected to continuous potential cycling from 1.0 to 1.7 V_{RHE} until reproducible voltagrams were obtained. To determine the resistance of the solution (R_s) electrochemical impedance spectroscopy (EIS) was measured at open circuit potential (OCP) in the frequency range 1 to 50, kHz. R_s was estimated from the resulting Nyquist plot and used for ohmic drop correction based on the relation $E_c = E_m - iR_s$, where E_c is, respectively, iR-corrected potential and E_m is the measured potential. The potentials were calibrated against a reversible hydrogen electrode (RHE). Linear sweep voltammetry (LSV) was conducted at a scan rate of 5 mV s^{-1} from 1.2 to 2.0, V_{RHE}. Cyclic voltammetry (CV) was used to measure the electrochemical effective surface area (ECSA). The test was performed in an O_2-saturated 1.0 M KOH solution to estimate the electrochemical double-layer capacitance (C_{dl}) at non-Faradaic overpotentials. CV scans were conducted at scan rates 20, 40, 60, 80, 100, and 120, mV s^{-1} over a voltage range 1.41 to 1.46, V_{RHE}. The difference in current density between the anodic and cathodic sweeps ($J_{anodic} - J_{cathodic}$) at 1.435 V_{RHE} was plotted as a function of the scan rate in which the slope is equal to twice the C_{dl} of the catalyst. Electrochemical impedance spectroscopy (EIS) was performed over a frequency range of 0.1 to 100, kHz under OCP and an applied voltage of 0.50, 0.52, 0.54, and 0.60, V with an ac perturbation of 10 mV.

Density Functional Theory Calculations: Density functional theory (DFT) calculations were performed using Vienna Ab initio Simulation Package (VASP) code within the generalized gradient approximation (GGA-PBE).[S1-S2] All were performed using a cut-off energy of 400 eV. For bulk and slab modeling a 2×2×2 expanded supercell from unitcell (96 atoms, Fig.1) was employed. For the slab model, an 18Å thick vacuum-layer was placed within the periodic cells repeated in the z-axis to obviate interactions. A supercell model of amorphous Co_2B with OH, O, OOH adsorptions on the surface Co atoms with coordination numbers of 1, 2, 3, and 4 was used in DFT modeling. Then, adsorption energy was calculated for the amorphous structures, where the strongest adsorption energies were used for the consideration of energy landscape.

In order to check the validity of DFT calculations on amorphous phase, binding energies between the surface Co and intermediates, such as OH, O, OOH, were calculated in three different supercell models with amorphous phase. The results showed that Co atoms in each amorphous Co_2B supercell having highest OH adsorption energy did not have exactly the same coordination number with B. However importantly, adsorption energy of OH was increased as coordination number of Co-B increases and the highest adsorption energies for three different amorphous Co_2B supercell models were similar as, -3.90, -3.94, -3.95 eV. In addition, the second highest adsorption energies in the three different supercell models of amorphous Co_2B were also very close to each other as -3.57, -3.56, and -3.54 eV. Thus, these results can support validity of our DFT calculations on the amorphous Co_2B system, although other factors still may exist which needs to be considered for further enhancing validity DFT calculations in amorphous materials..[S3-S5]

***Calculation of turnover frequency (TOF)*:** TOF is calculated from,

$$TOF = j \times \frac{A}{4 \times F \times N_s}$$

where j, A, F and N_s are, respectively, current density at a certain overpotential (A cm^{-2}), surface area of the working electrode (cm^{-2}), Faraday constant (96,458 C mol^{-1}), and concentration of activie sites in the catalsyts (mol cm^{-2}). N_s for oxygen evolution reaction (OER) was determined by CV measurments at different scan rates in the voltage range where redox reaction occurs. The peak current is plotted against scan rate where the slope has the linear relationship,

$$Slope = n^2F^2AN_S/4RT$$

in which n, R, and T are, respectively, the number of electrons transferred (here $n = 1$), ideal gas constant and absolute temperature.[S6-S8] The linear relationship between N_S and scan rate was derived from the Nernst equation,

$$E = E^{0'} + \frac{RT}{nF} ln \frac{C_{ox}(t)}{C_{red}(t)}$$

where $E^{0'}$ and C(t) are the potential of redox species and the time-dependent concentrations of redox producs, respectively. Assuming that there is no bulk concentration, the current (i) can be obtained as the concentration variation of the oxidized species,

$$i = -nFV\left[\frac{dC_{ox}(t)}{dt}\right]$$

where n = number of transfer electrons, V and t are volume and time, respectively. Given the constant of the total concentration,

$$C_T = C_{ox}(t) + C_{red}(t)$$

$C_{ox}(t)$ can be described as follow,

$$C_{ox}(t) = \frac{C_T exp\left[\frac{nF(E - E^{0'}}{RT}\right]}{1 + exp\left[\frac{nF(E - E^{0'}}{RT}\right]}$$

by differentiating the equation of $C_{ox}(t)$ with respect to t and substituting into equation of i, the i can be obtained as,

$$i = \frac{n^2F^2VC_T\nu}{RT}\frac{exp\left[\frac{nF(E - E^{0'}}{RT}\right]}{\left\{1 + exp\left[\frac{nF(E - E^{0'}}{RT}\right]\right\}^2}$$

where ν is the scan rate, which is equal to $-\frac{dE}{dt}$. Since $E = E^{0'}$ at peak current, and VC_T can be replaced by AN_S, finally we can get,

$$i = \frac{n^2F^2AN_S\nu}{4RT}$$

Hence, the linear relationship between the oxidation peak current and scan rate can be used to estimate the number of redox active sites.

***Determination of collection efficiency for RRDE*:**

The collection efficiency of RRDE system was calibrated in 0.1 M KOH with a 10 mM potassium ferricyanide, $K_3Fe(CN)_6$, electrolyte. The ferrocyanide/ferricyanide half reaction is a simple and single-electronic reaction that is frequently used as the standard method for calculating collection efficiency of RRDE system.

$Fe(CN)^{3-}_{6} + e^{-} \rightarrow Fe(CN)^{4-}_{6}$ (Reduction of ferricyanide)

$Fe(CN)^{4-}_{6} + e^{-} \rightarrow Fe(CN)^{3-}_{6}$ (Oxidation of ferrocyanide)

Initially, both ring and disk electrodes were fixed at sufficiently positive potential, and then the potential sweep towards negative voltage were performed on the disk electrode with scan rate of 10 mV s^{-1}. The potential of ring electrode was fixed at a positive potential (oxidizing) and rotation speed was held at 500, 1000, and 1600 rpm during the measurement. Figure Rxx shows the collected voltage-current plots at the both of ring and disk electrodes. The collection efficiency of RRDE system was calculated by the measured ratio of the ring limiting current to the disk limiting current (Fig.Sxx), which was about 0.2005.

$$N_{collection\ efficienty} = - i_{limiting,ring} / i_{limiting,disk}$$

***Ultraviolet Photoelectron Spectroscopy*:** Work function analysis was conducted using ultraviolet photoelectron spectroscopy (UPS; Thetaprobe; Thermo).

X-ray Absorption Spectroscopy: X-ray absorption spectroscopy (XAS) of the powder samples was measure at 1D KIS-PAL XAS beamline at the Pohang Light Source (PLS-II) equipped with bending magnet and operated at an energy of 3.0 GeV with a maximum storage current of 300 mA. The beamline comprised a double-crystal Si (111) monochromator detuned to 40% to suppress higher order harmonic content from the beam. The beamline is operating in an energy range of 4 to 16 KeV with an energy resolution (ΔE/E) of 2×10^{-4}. The optical components consist of a tangential focusing and collimating mirror. The beam size was 2 (horizontal) × 1 (vertical) mm (focused) during XAS measurements. The data were collected in transmission mode with argon-nitrogen gas-filled ionization chambers as detectors. Co metallic reference foil was also measured simultaneously to calibrate the data. The data were analyzed using the ATHENA software package. [S9] The EXAFS data was plotted in the *k*-range of 0.2 to 1.0 nm^{-1} with k^2-weight in Hanning window and in an R-range of 0 to 0.6 nm. Fourier transformation (FT) of the EXAFS oscillations were plotted without phase-correction and the actual bond lengths are longer with a shift in x-axis than the plotted.

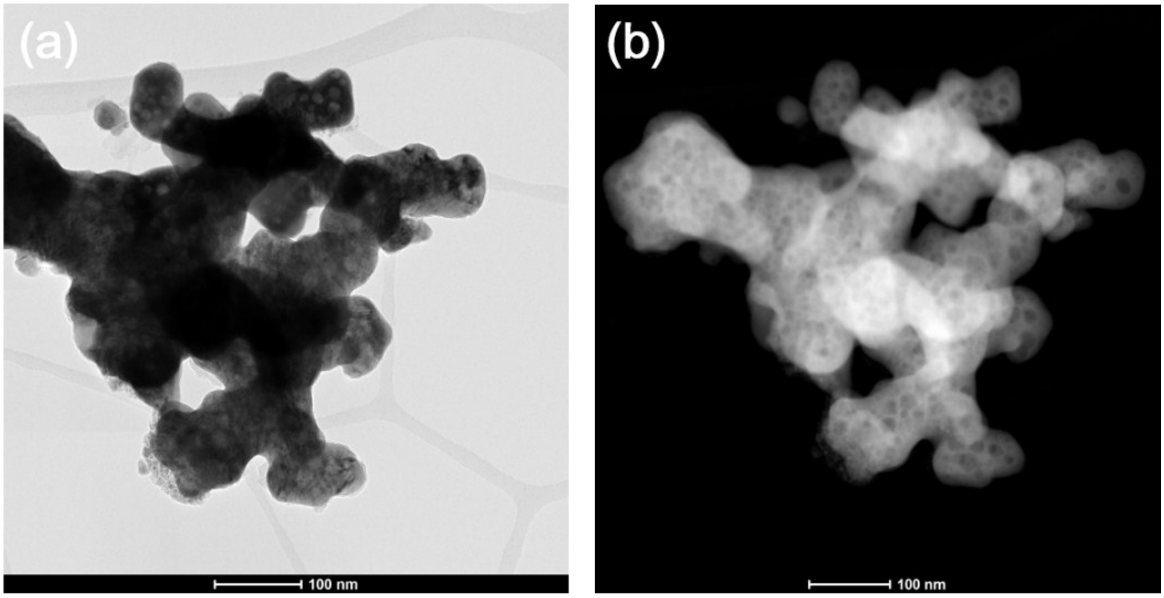

Figure S1. Low-resolution TEM images of F-Co_2B, a) bright-field, b) dark-field.

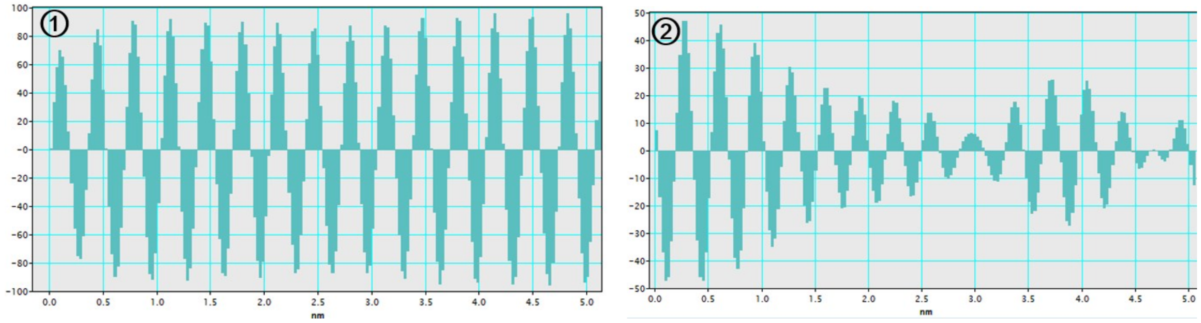

Figure S2. Line profiles for marked regions as "1" and "2".

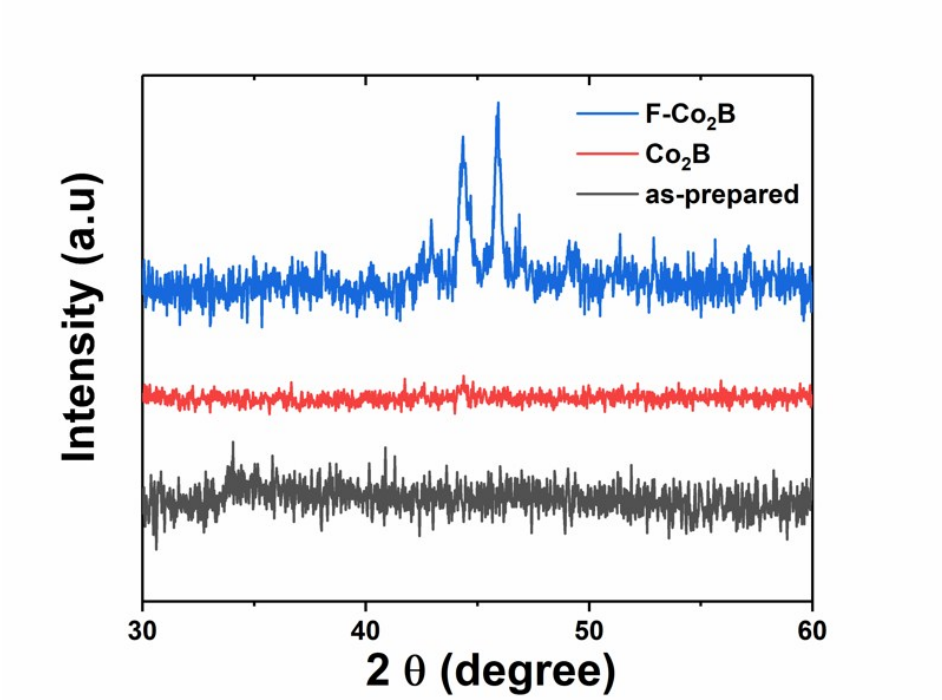

Figure S3. XRD patterns for F-Co$_2$B, Co$_2$B and the as-prepared samples.

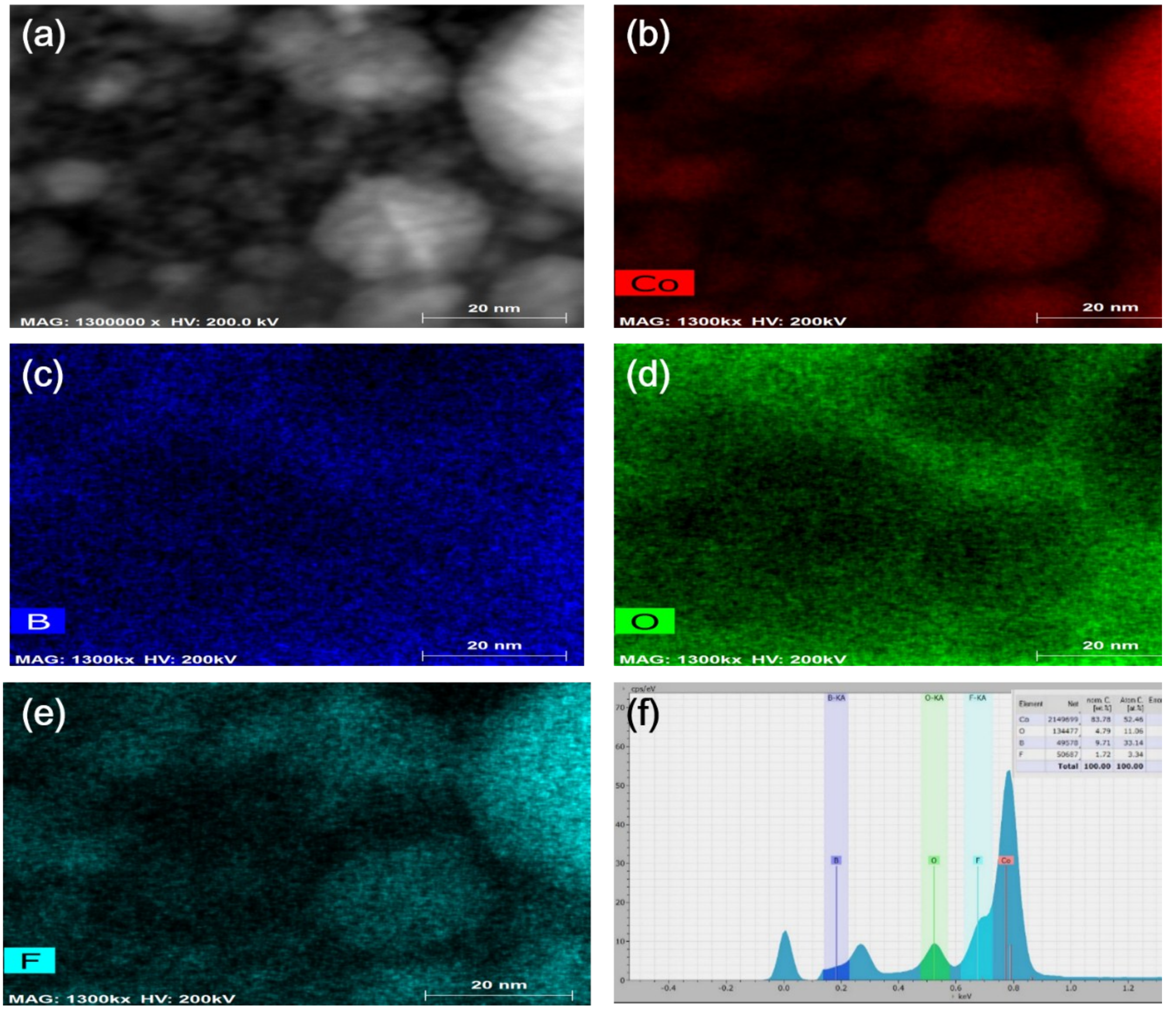

Element	Net	norm. C. [wt.%]	Atom C. [at.%]	Erro
Co	2149699	83.78	52.46	
O	134477	4.79	11.06	
B	49578	9.71	33.14	
F	50687	1.72	3.34	
	Total	100.00	100.00	

Figure S4. a) Dark-field TEM image and corresponding EDX mapping image for b) Co (red), c) B (blue), d) O (green) and e) F (cyan) elements for F-Co_2B with f) quantitative mapping results.

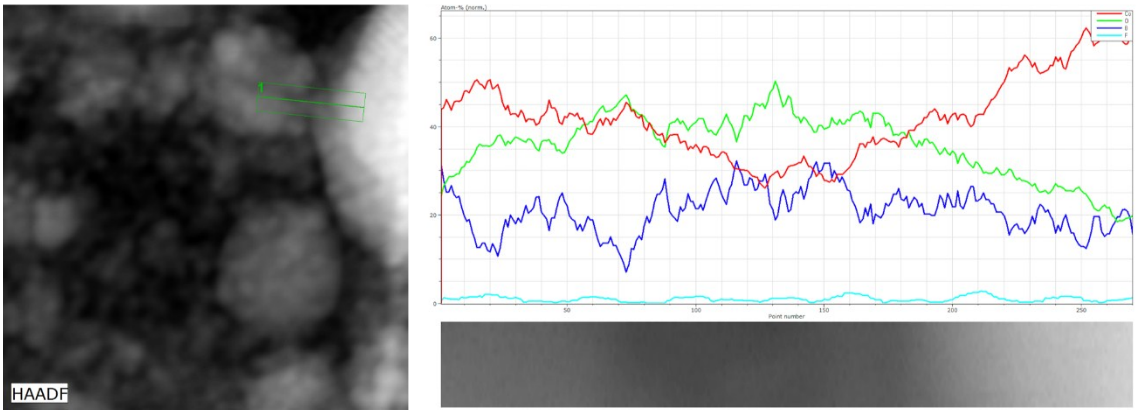

Figure S5. EDX line profile across the c-a interface of F-Co_2B. Red and green lines are Co and O, respectively.

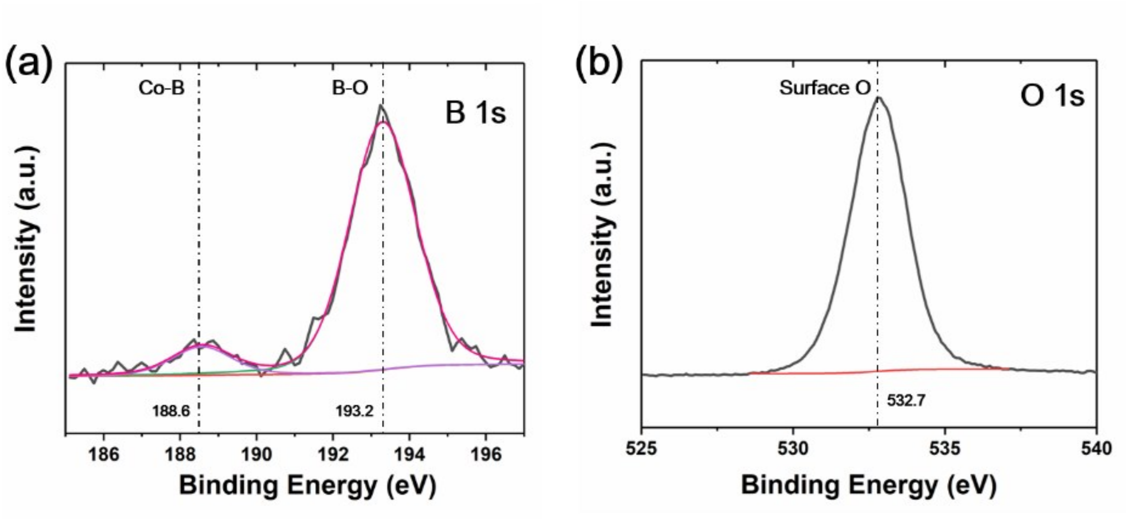

Figure S6. XPS spectra for a) B 1s and b) O 1s for F-Co_2B.

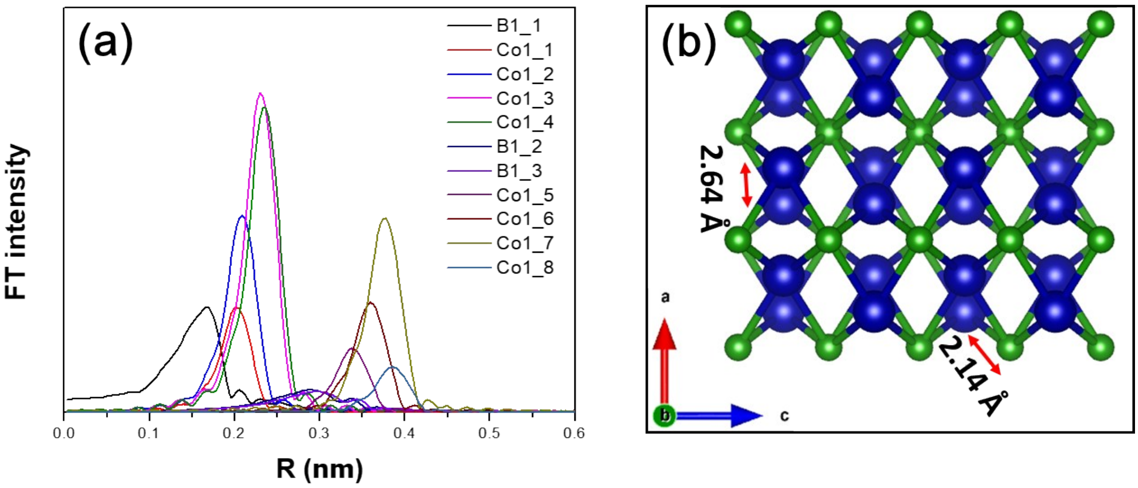

Figure S7. Theoretically generated scattering paths for Co_2B without phase-corrected. (b) The crystal structure of Co_2B where Co atoms are shown in blue and B atoms in green color.

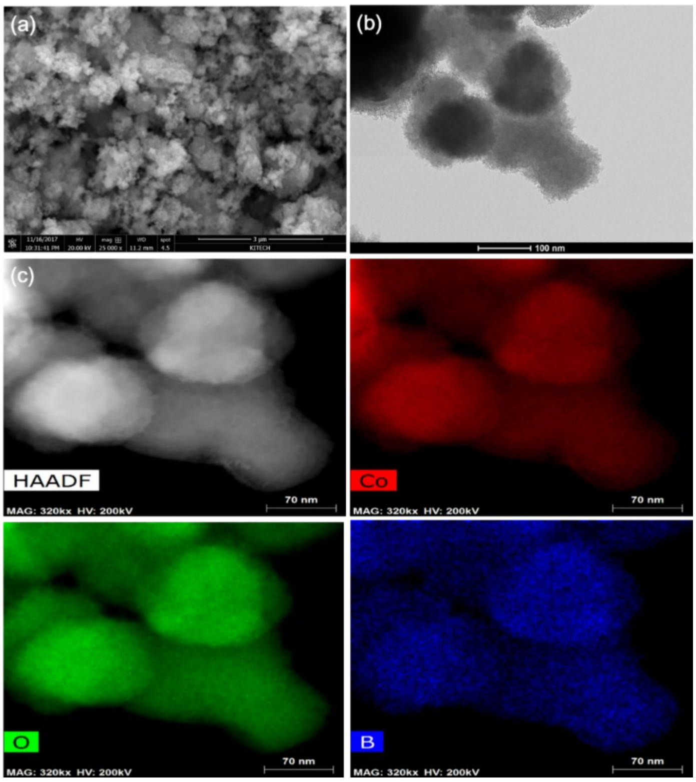

Figure S8. a) SEM image of Co_2B b) Low-resolution TEM image of Co_2B and corresponding EDS mapping images for Co, O, and B.

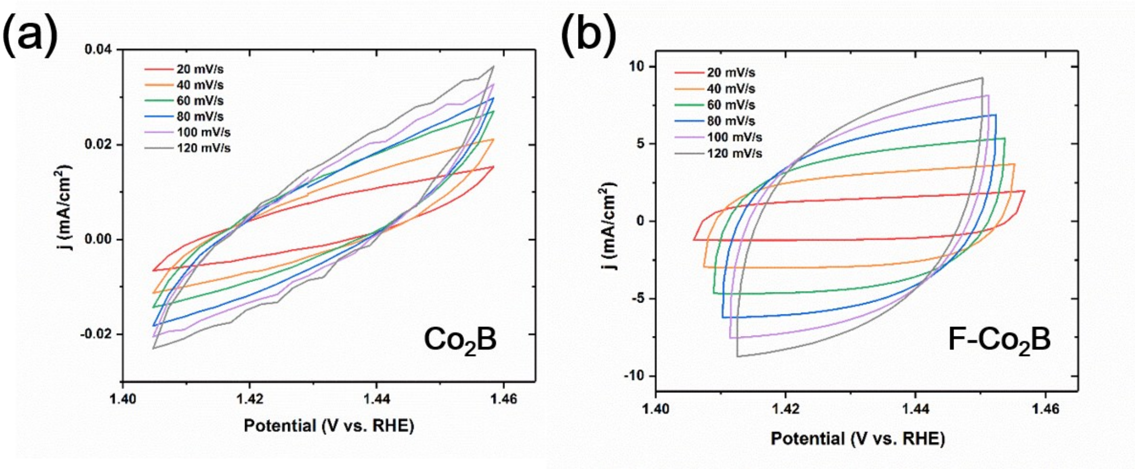

Figure S9. CV scans measured at a voltage range from 1.40 to 1.46 V_{RHE} (no *iR*-compensation), where a capacitive current flows, with scan rates, respectively, 20, 40, 60, 80, 100 and 120, mV s^{-1} for a) Co_2B and b) F-Co_2B.

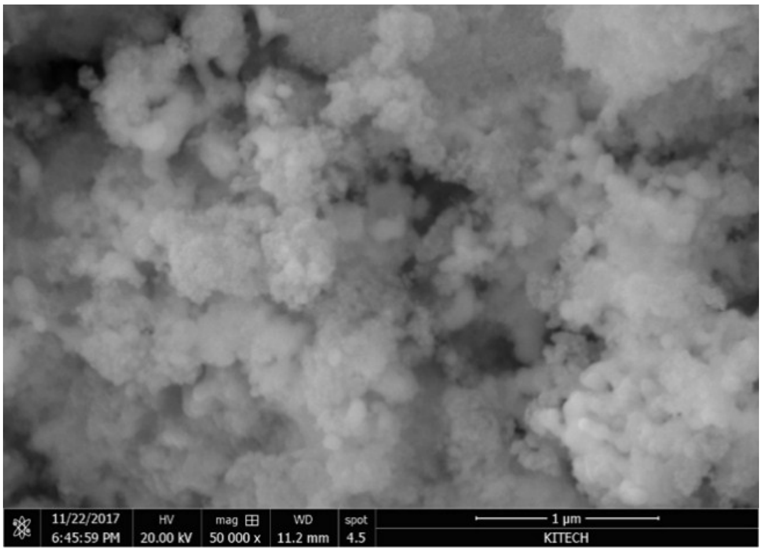

Figure S10. SEM image of F-Co_2B.

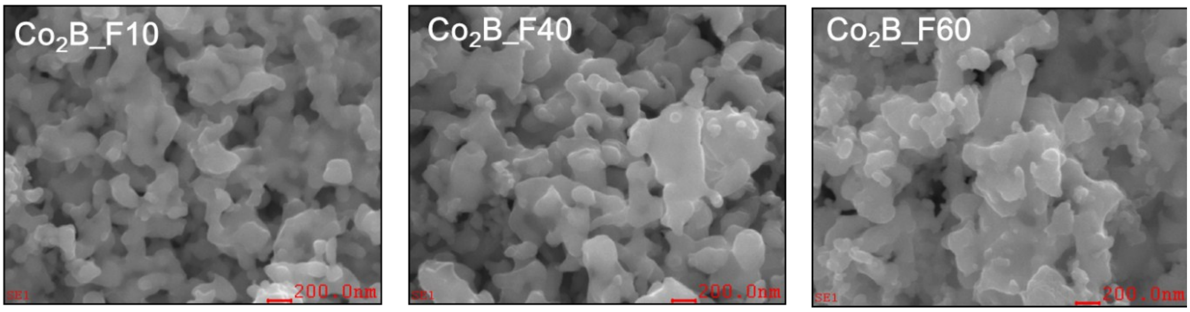

Figure S11. SEM images of F-Co$_2$B with varying F (respectively, 15, 40 and 60, %).

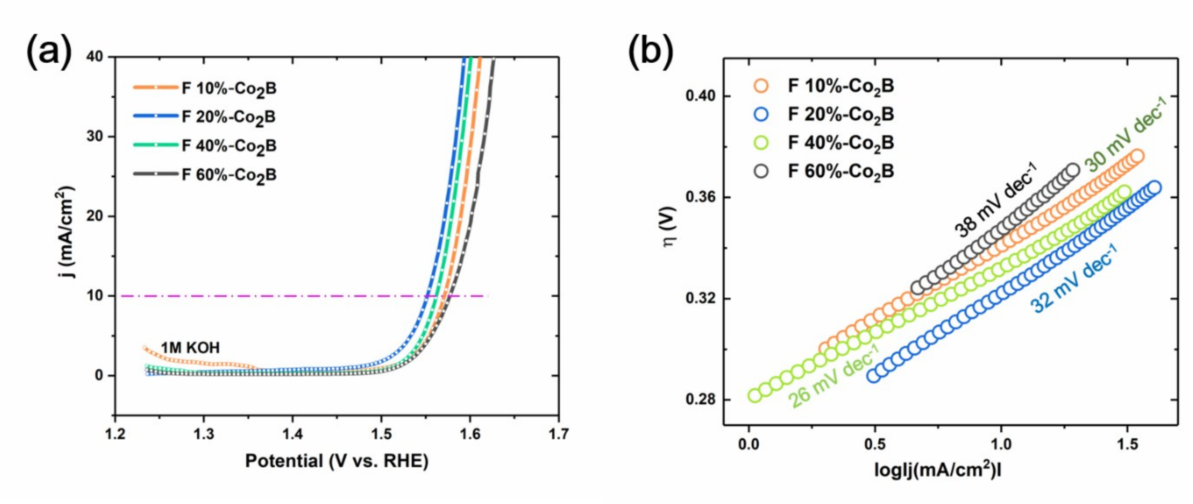

Figure S12. a) LSV curves (scan rate 5 mV s^{-1}) for F-Co$_2$B with varying F and b) corresponding Tafel plots measured in 1M KOH solution.

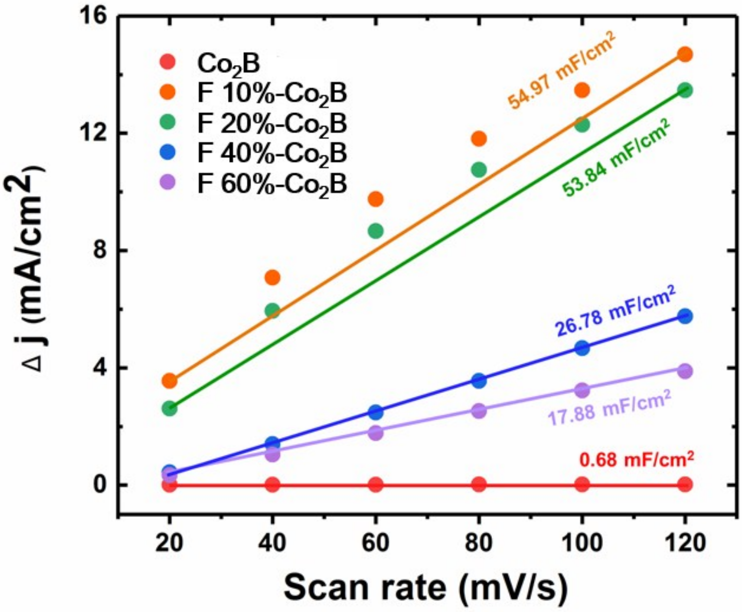

Figure S13. Computed C_{dl} values using CV data measured in a capacitive region (1.40 to 1.46 $V_{RHE,}$ no *iR*-compensation) at scan rates, respectively, 20, 40, 60, 80, 100 and 120, mV s^{-1} in 1 M KOH solution.

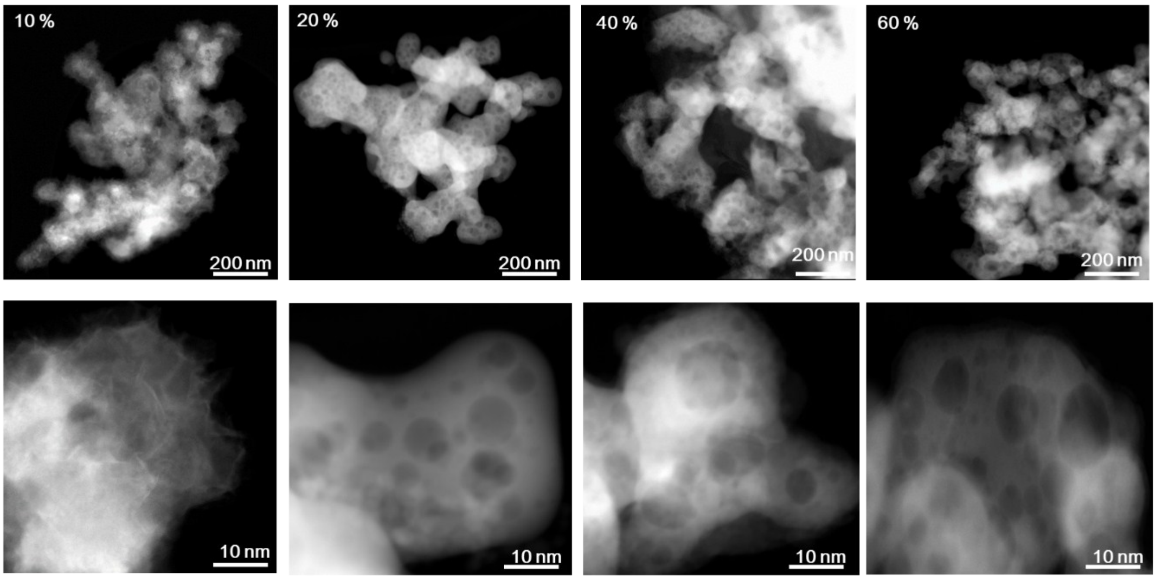

Figure S14. Low-resolution dark-filed TEM images of F-Co$_2$B with different F amounts.

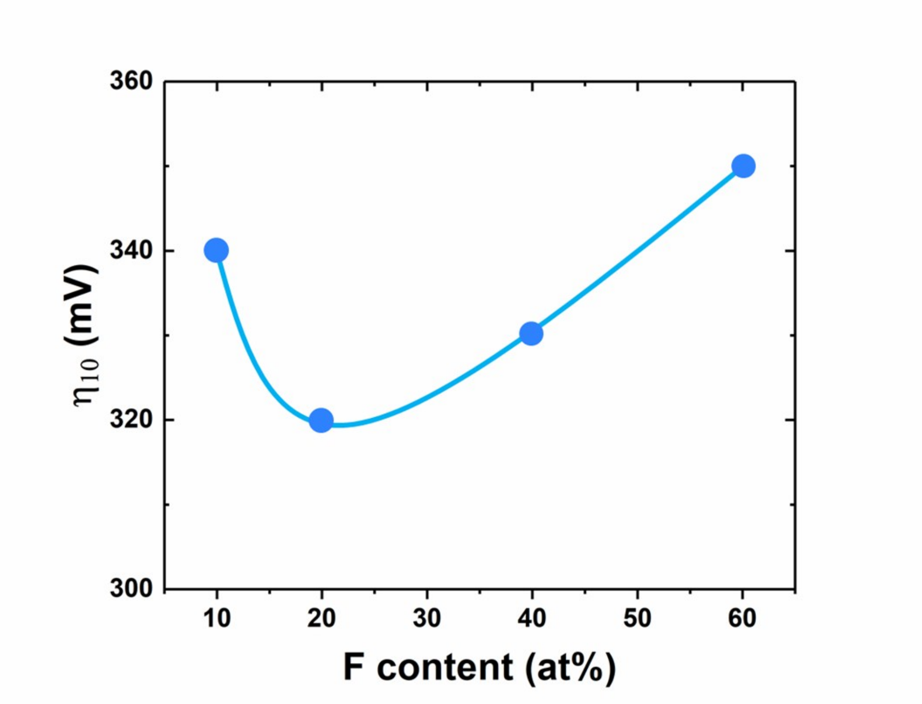

Figure S15. Overpotential for affording a current density of 10 mA cm^{-2} of F-Co_2B catalysts with different F amounts.

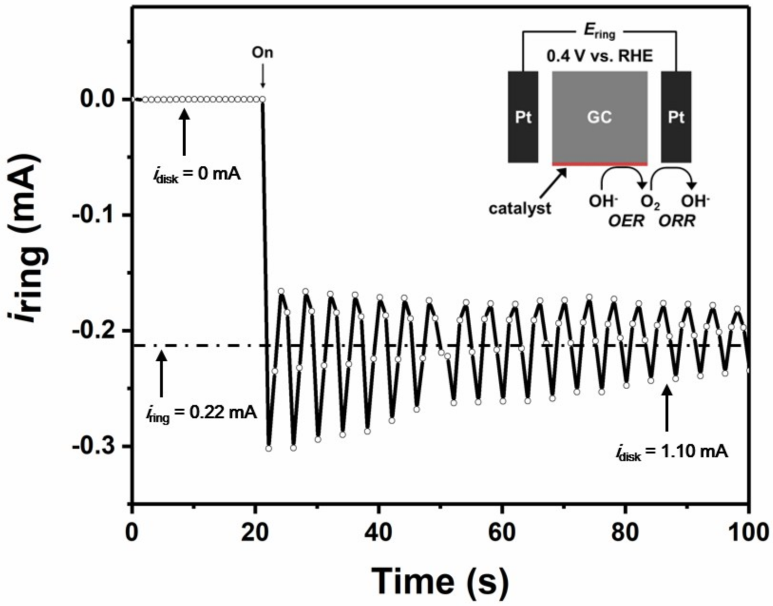

Figure S16. RRDE data for F-Co_2B. (Inset shows schematic of the experimental set-up).

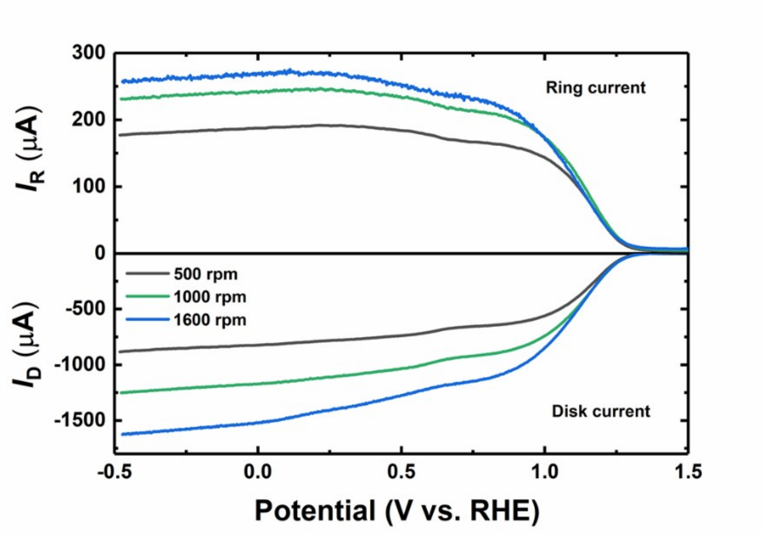

Figure S17. LSV-RRDE calibration curves for calculation of a collection efficiency (N) using 0.1 M KOH with 10 mM $K_3Fe(CN)_6$.

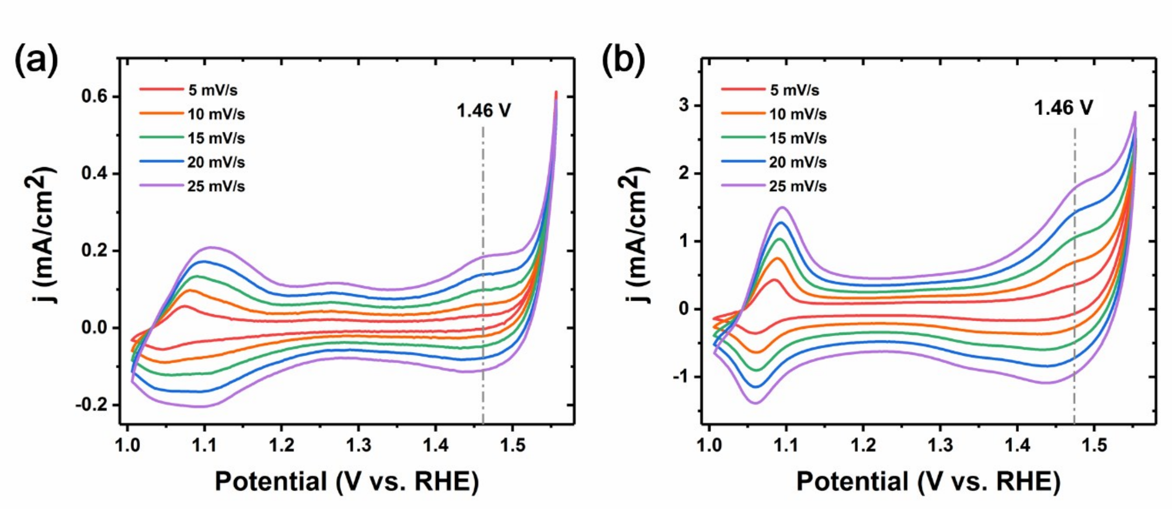

Figure S18. CV of a) F-Co_2B and b) Co_2B at different scan rates of 5, 10, 15, 20 and 25, mV s^{-1} in 1 M KOH.

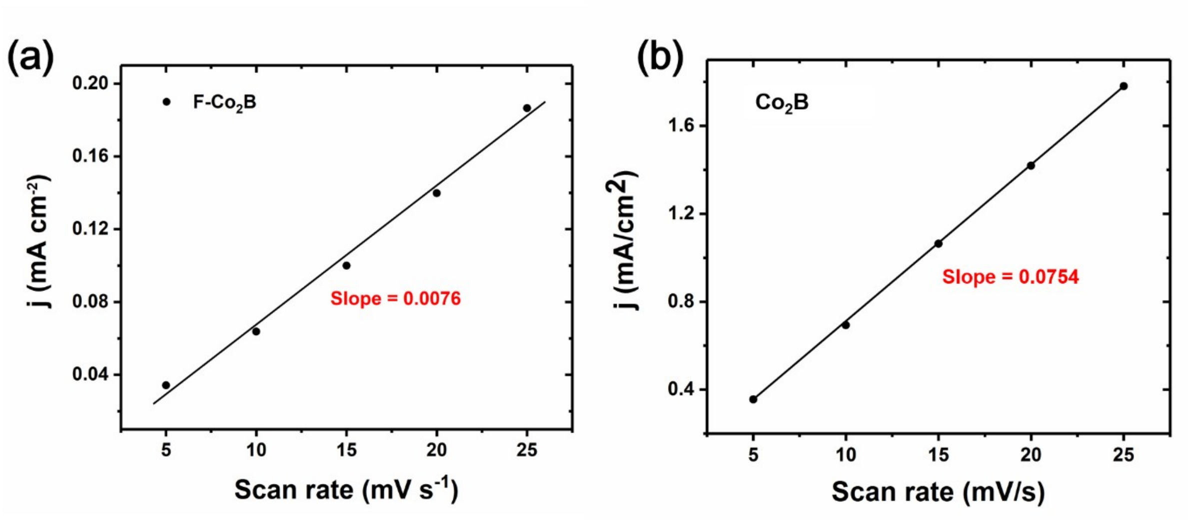

Figure S19. Linear relationship of the oxidation peak currents vs. scan rate at 1.46 V in the CVs (Fig. S12) for a) F-Co_2B and b) Co_2B.

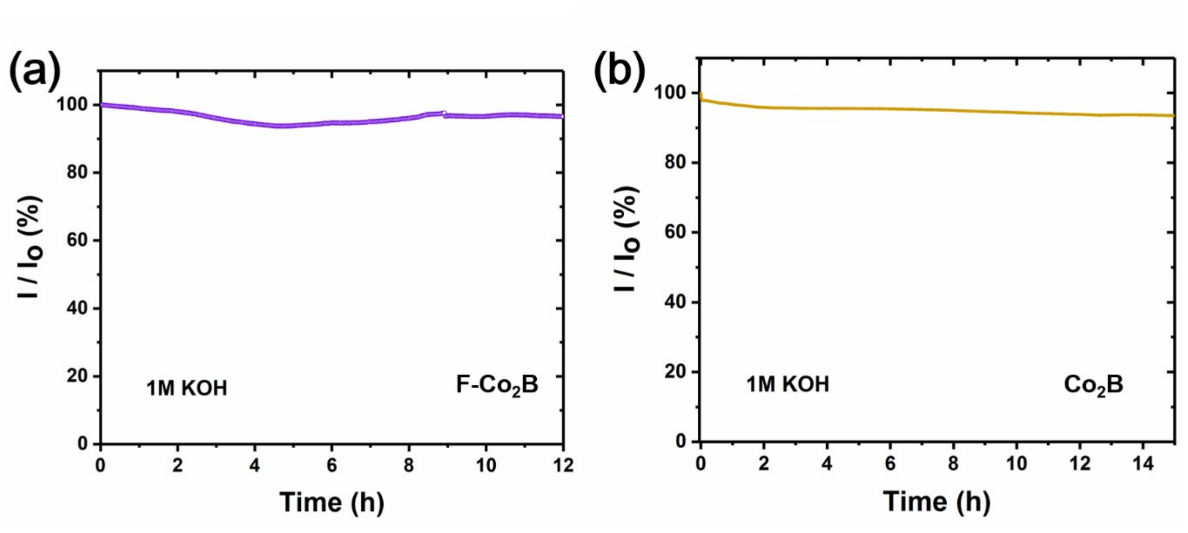

Figure S20. Chronoamperometry curves for a) F-Co2B and b) Co2B under an applied voltage 1.55 V_{RHE} in 1M KOH.

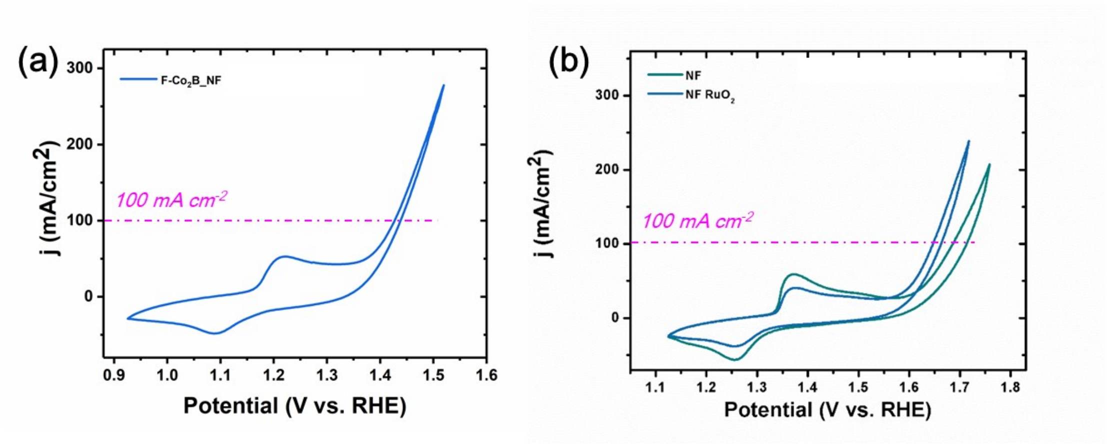

Figure S21. CV cycle of F-Co$_2$B loaded on nickel foam, RuO$_2$ loaded on nickel foam, and bare nickel foam, respectively. Measurements were performed 1.0 M KOH solution with a scan rate of 5 mV s^{-2}.

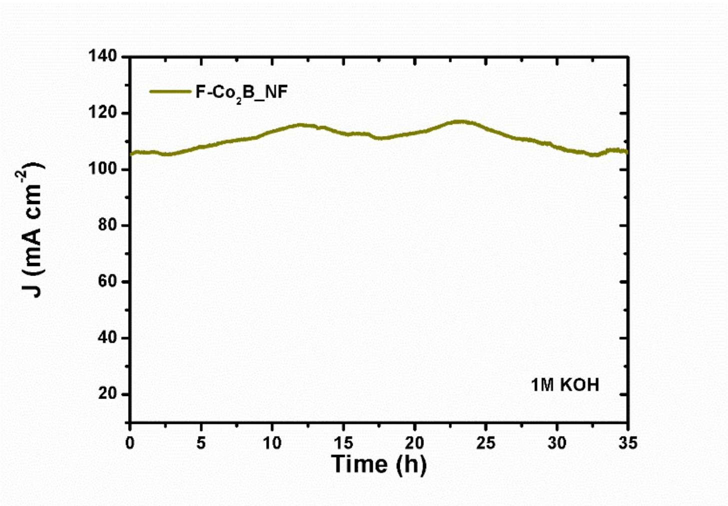

Figure S22. Chronoamperometry curve for F-Co2B loaded on nickel foam generating at a constant voltage for generating an current density of about 100 mA cm^{-2} in 1M KOH under applied voltage of 1.43 V$_{RHE}$.

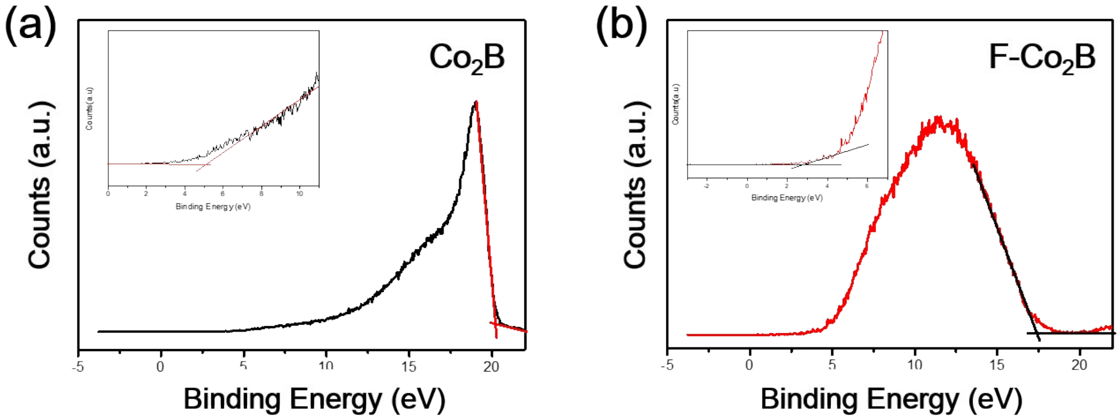

Figure S23. UPS spectra of a) Co$_2$B and b) F-Co$_2$B for computing work functions.

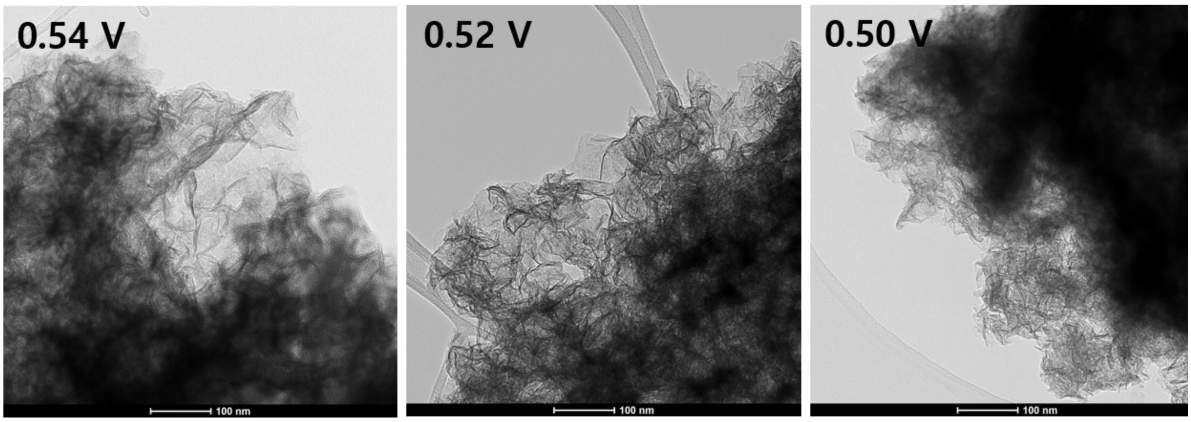

Figure S24. TEM images of F-Co$_2$B after 20 min OER under varying (0.54 to 0.50) applied voltage.

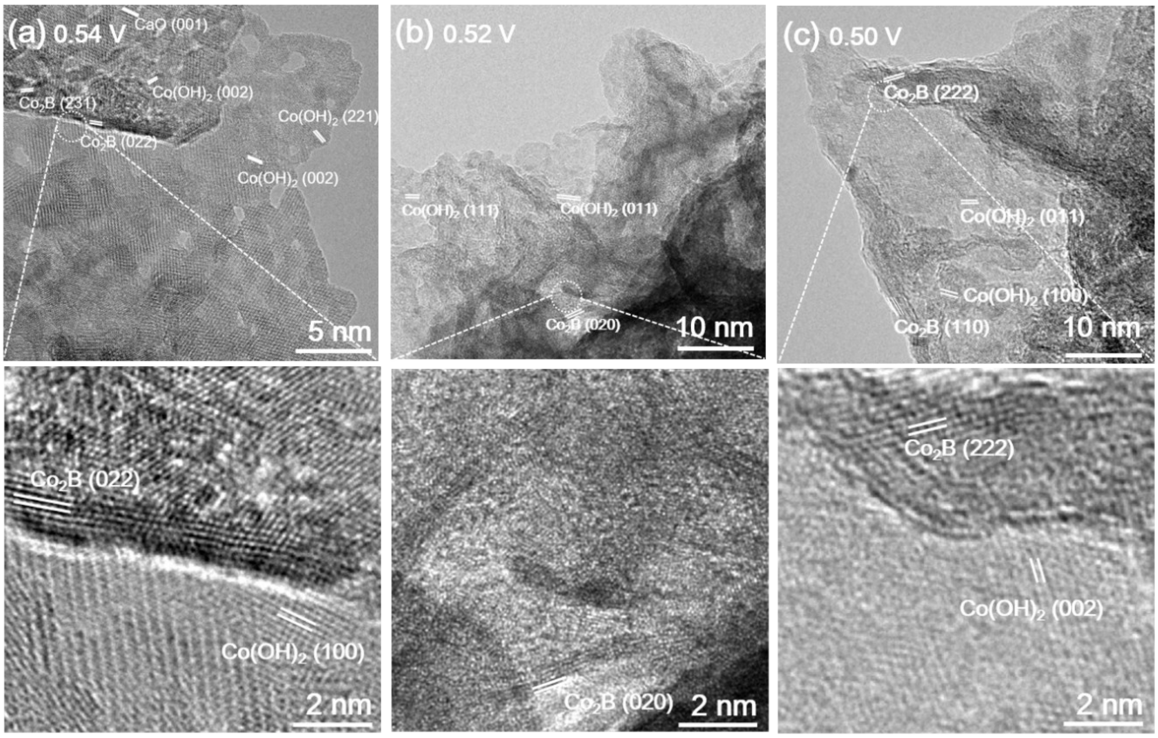

Figure S25. *Ex-situ* HR-TEM images for F-Co_2B after 20 min OER under varying (0.54 to 0.50) applied voltage.

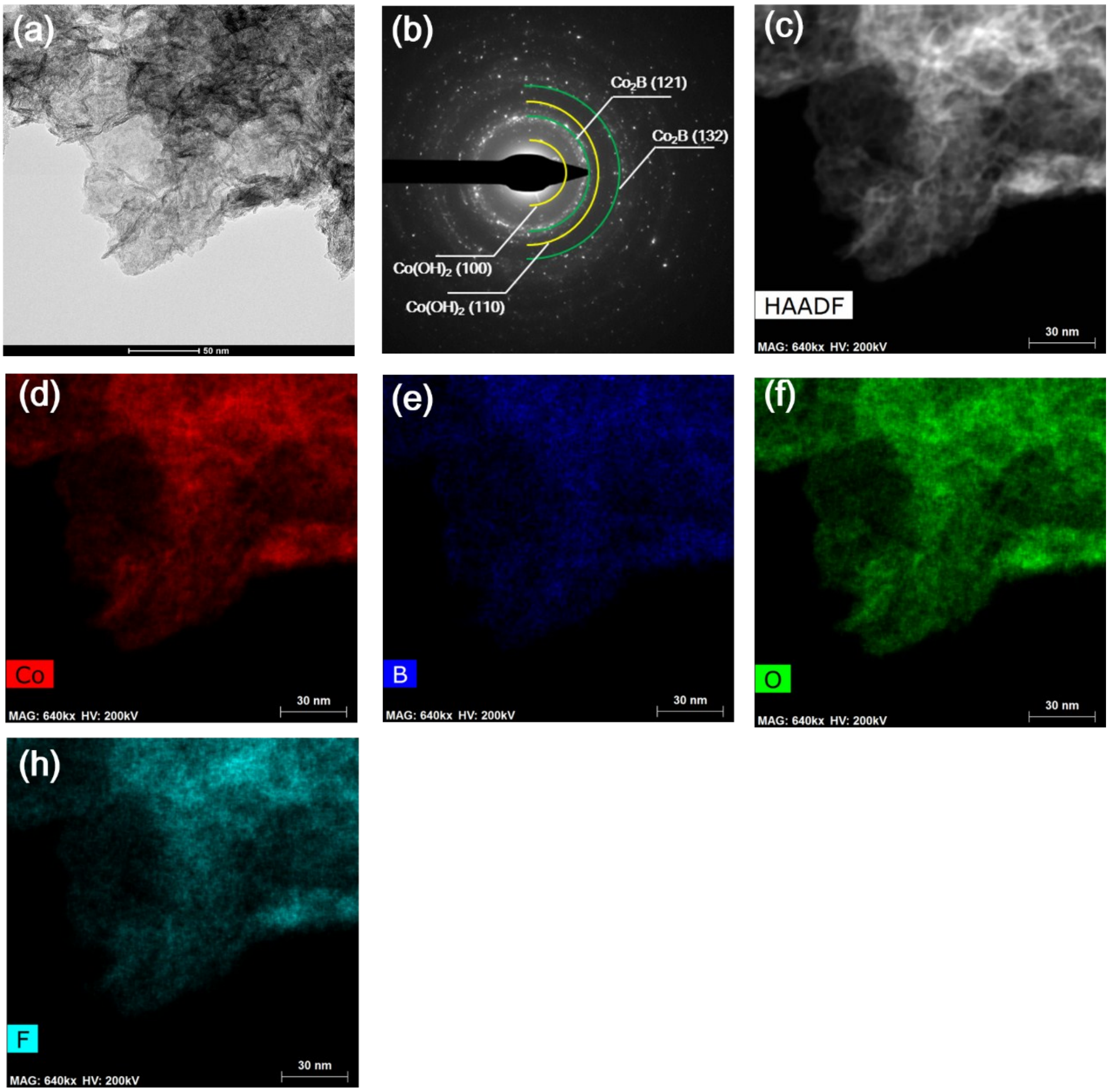

Figure S26. a,b) Low and high-resolution TEM and SAED pattern images for F-Co$_2$B following 10 h electrocatalytic water oxidation in 1 M KOH c-h) Corresponding elemental (Co, O, B, and F) mapping images.

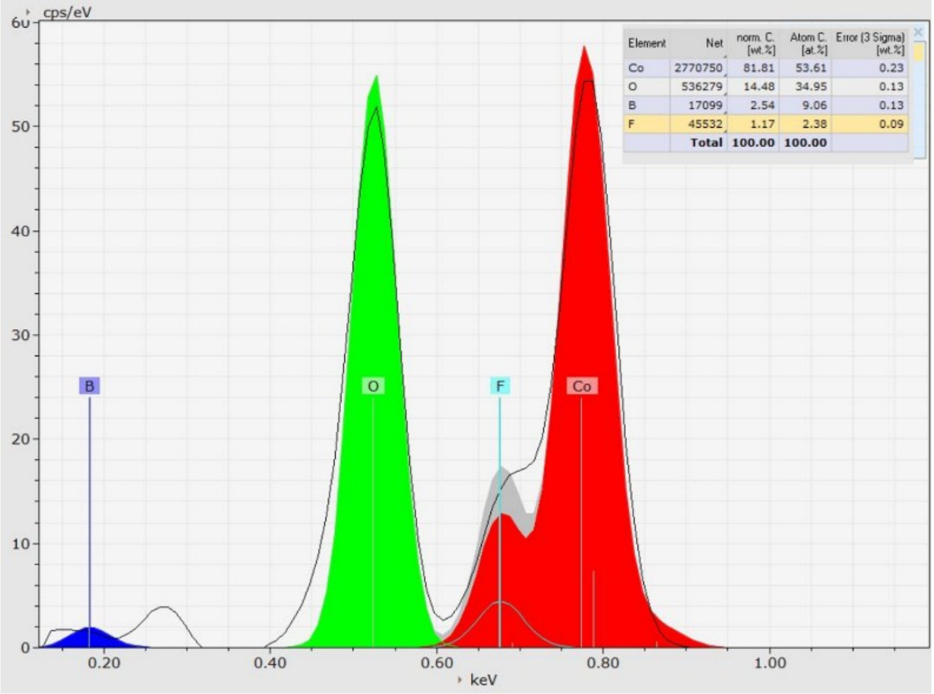

Element	Net	norm. C. [wt.%]	Atom C. [at.%]	Error (3 Sigma) [wt.%]
Co	2770750	81.81	53.61	0.23
O	536279	14.48	34.95	0.13
B	17099	2.54	9.06	0.13
F	45532	1.17	2.38	0.09
	Total	**100.00**	**100.00**	

Figure S27. Quantitative analysis for EDS mapping data (Fig. S17d) for post-OER F-Co_2B.

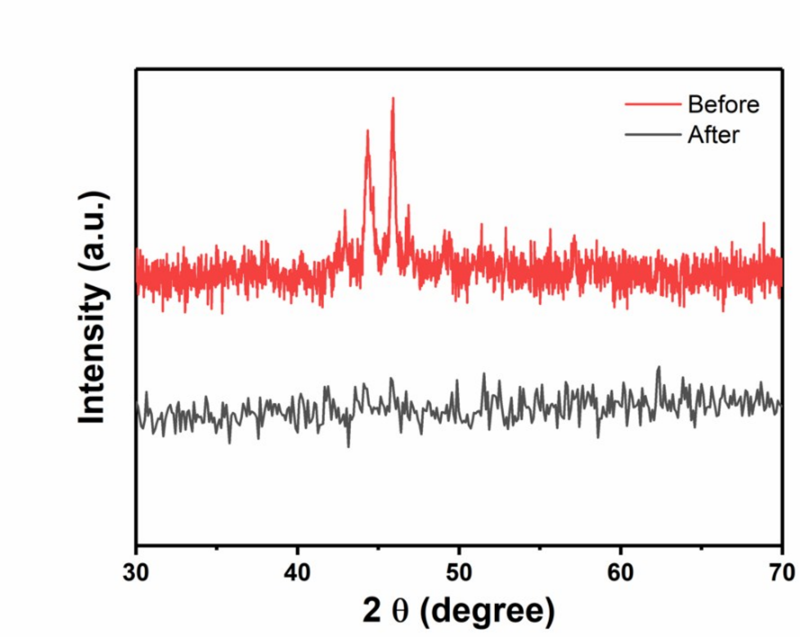

Figure S28. XRD pattern for F-Co_2B before and after 10 h OER in 1 M KOH.

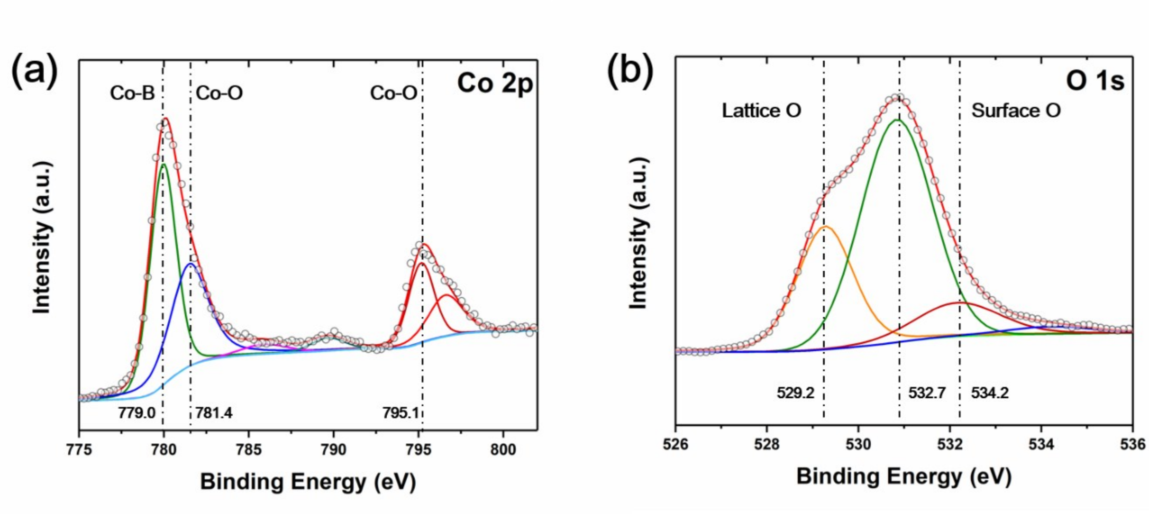

Figure S29. XPS spectra of a) Co 2p and b) O 1s for F-Co_2B following long-term (12 h) OER in 1 M KOH.

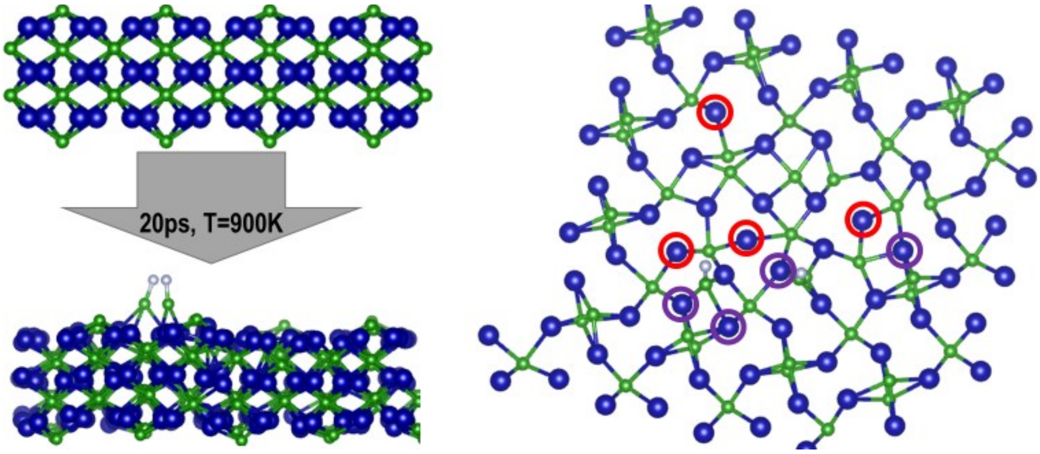

Figure S30. Changed coordinate number of amorphous Co_2B from 3 to 2(red circles) and 4(purple circles) (right). Blue, green and grey spheres indicate Co, B, and F atoms, respectively.

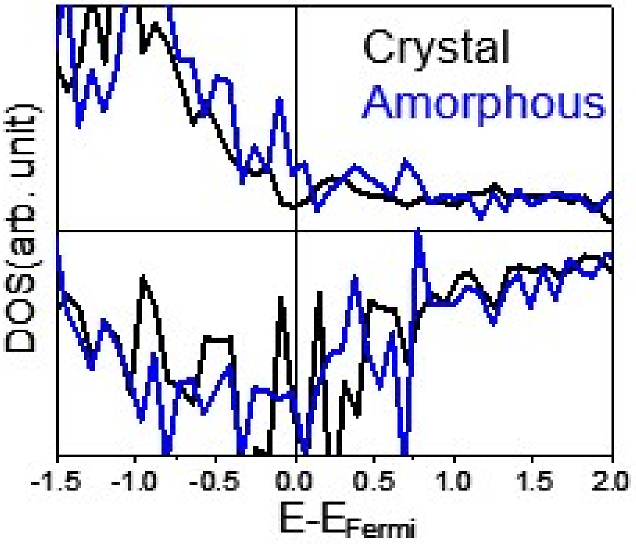

Figure S31. Calculated DOS for crystal (black line) and amorphous (blue line) Co_2B phases, respectively.

Table S1. A comparison of catalytic OER activity for F-Co2B with transition metal borides, sulfides, selenides and phosphides in alkaline media.

Catalyst	Electrolyte	*η^{10} (mV)	**η^{100} (mV)	Tafel slope (mV dec^{-1})	Loading amount (mg cm^{-2})	Reference
F-Co_2B	1 M KOH	320	-	32	0.28	This work
F-Co_2B/NF	1 M KOH	-	170	-	0.85	This work
Co_2B-500	0.1 M KOH	380	-	45	0.21	S10
Ni_xB-300	1 M KOH	380	-	89	0.21	S11
Ni-B/NF	1 M KOH	360	-	76	12.3	S12
Co-3Mo-B	1 M KOH	320	-	155	2.1	S13
$Co_2B/CoSe_2$	1 M KOH	320	-	56	0.4	S14
Co-Ni-B@NF-500	1 M KOH	313	-	120	-	S15
Ni-B_i@NB	1 M KOH	302	-	52	0.3	S16
Co_9S_8@MoS_2/CNFs	1 M KOH	430	-	61	0.212	S17
NiCoS/CC NSs	1 M KOH	330	-	109	-	S18
$NiCo_2S_4$ NA/CC	1 M KOH	340	-	89	0.43	S19
NiSe/NF	1 M KOH	400	-	N/A	2.8	S20
CP@FeP	1 M KOH	365	-	63	0.7	S21
NiCoP/NF	1 M KOH	280	-	87	1.6	S22
Ni@Ni/C-400	1 M KOH	-	450	87	7.3	S23
NiNO/CC	1 M KOH	-	390	54	0.38	S24
$NiCo_2S_2$ NW/NF	1 M KOH	-	370	74	-	S25
Ni_2P@NF-6	1 M KOH	-	590	40	3.5	S26
Ni@Co-Ni-P	1 M KOH	-	380	297	3.0	S27

*Overpotential for affording a current density of 10 mA cm^{-2}; **Overpotential for affording a current density of 100 mA cm^{-2}.

References for SI

[S1] J. P. Perdew, K. Burke, M. Ernzerhof, *Phys. Rev. Lett.* 1997, **78**, 1396.

[S2] L. G. Ferreira, M. Marques, L. K. Teles, *Phys. Rev. B.* 2008, **78**, 125116.

[S3] L. R. L. ing, Y. Deng, L. Ma, Y. Zhang, A. A. Peterson, B. S. Yeo, *ACS Catal.* 2016, **6**, 861-867.

[S4] H. Jiao, Y. Li, B. Delmon, J. Halet, *J. Am. Chem. Soc.* 2001, **123**, 7334-7339.

[S5] P. I. Ravikovitch, A. V. Neimark, *Langmuir* 2006, **22**, 11171-11179.

[S6] W. S. Jiang, X. P. Zong, L. An, S. X. Hua, X. Miao, S. L. Luan, Y. J. Wen, F. F. Tao, Z. C. Sun, *ACS Catal.* 2018, **8**, 2209.

[S7] S. Pintado, S. Goberna-Ferron, E. C. Escudero-Adan, J. R. Galan-Mascaros, *J. Am. Chem. Soc.* 2013, **135**, 13270.

[S8] Y. Li, L. Zhang, X. Xiang, D. P. Yan, F. Li, *J. Mater. Chem. A.* 2014, **2**, 13250.

[S9] B. Ravel, M. Newville, *J. Synchrotron Radiat.* 2005, **12**, 537.

[S10] J. Masa, P. Weide, D. Peeters, I. Sinev, W. Xia, Z. Sun, C. Somsen, M. Muhler, W. Schuhmann, Adv. Energy Mater. 2016, 6, 1502313.

[S11] J. Masa, I. Sinev, H. Mistry, E. Ventosa, M. Mata, J. Arbiol, M. Muhler, B. Cuenya, W. Schuhmann, Adv. Energy Mater. 2017, 7, 1700381.

[S12] Y. Liang, X. Sun, A. Asiri, Y. He, Nanotechnology, 27 (2016) 12LT01.

[S13] S. Gupta, N. Patel, R. Fernandes, S. Hanchate, A. Miotello, D.C. Kothari, Electrochimica Acta, 232 (2017) 64–71.

[S14] Y. Guo, Z. Yao, C. Shang, E. Wang, ACS Appl. Mater. Interfaces 2017, 9, 39312−39317.

[S15] N. Xu, G. Cao, Z. Chen, Q. Kang, H. Dai, P. Wang, J. Mater. Chem. A, 2017, 5, 12379.

[S16] W. Jiang, S. Niu, T. Tang, Q. Zhang, X. Liu, Y. Zhang, Y. Chen, J. Li, L. Gu, L. Wan, J. Hu, Angew. Chem. Int. Ed. 2017, 56, 6572-6577.

[S17] H. Zhu, J. F. Zhang, R. P. Yanzhang, M. L. Du, Q. F. Wang, G. H. Gao, J. D. Wu, G. M. Wu, M. Zhang, B. Liu, J. M. Yao, X. W. Zhang, Adv Mater 2015, 27, 4752.

[S18] C. Tang, Z. H. Pu, Q. Liu, A. M. Asiri, Y. L. Luo, X. P. Sun, Int J Hydrogen Energ 2015, 40, 4727

[S19] D. N. Liu, Q. Lu, Y. L. Luo, X. P. Sun, A. M. Asiri, Nanoscale 2015, 7, 15122

[S20] C. Tang, N. Y. Cheng, Z. H. Pu, W. Xing, X. P. Sun, Angew Chem Int Edit 2015, 54, 9351

[S21] D. H. Xiong, X. G. Wang, W. Li, L. F. Liu, Chem Commun 2016, 52, 8711

[S22] H. Liang, A. N. Gandi, D. H. Anjum, X. Wang, U. Schwingenschlogl, H. N. Alshareef, *Nano Lett.* **2016**, *16*, 7718.

[S23] H. Sun, Y. Lian, C. Yang, L. Xiong, P. Qi, Q. Mu, X. Zhao, J. Guo, Z. Deng, Y. Peng, *Energy Environ. Sci.**, 2018**, 11, 2363*

[S24] J. Huang, Y. Sun, X. Du, Y. Zhang, C. Wu, C. Yan, Y. Yan, G. Zou, W. Wu, R. Lu, Y. Li, J. Xiong, *Adv. Mater., **2018**, 30, 1803367*

[S25] A. Sivanantham, P. Ganesan, S. Shanmugam, *Adv. Funct. Mater., **2016**, 26, 4661−4672*

[S26] J. Zheng, W. Zhou, T. Liu, S. Liu, C. Wang, L. Guo, *Nanoscale, **2017**, 9, 4409-4418*

[S27] W. Li, X. Gao, X. Wang, D. Xiong, P. Huang, W. Song, X. Bao, L. Liu, *Journal of Power Sources,* **2016,** 330, 156-166.